Electronic Supplementary Material (ESI) for Nanoscale.
This journal is © The Royal Society of Chemistry 2021

Electronic Supplementary Information

Atomic Ni and Cu co-anchored 3D nanoporous graphene as an efficient oxygen reduction electrocatalyst for zinc-air batteries

*Yongtai Cheng [a, †], Haofei Wu [a, †], Jiuhui Han [b, c, †], Siying Zhong [d], Senhe Huang [e], Shufen Chu [a], Shuangxi Song [a], Kolan Madhav Reddy [a], Xiaodong Wang [a], Shaoyi Wu [d], Xiaodong Zhuang [e], Isaac Johnson [c, f], Pan Liu [a, *], Mingwei Chen [f, *]*

[a] Shanghai Key Laboratory of Advanced High-temperature Materials and Precision Forming, State Key Laboratory of Metal Matrix Composites, School of Materials Science and Engineering, Shanghai Jiao Tong University, Shanghai 200240, P. R. China

[b] Frontier Research Institute for Interdisciplinary Sciences (FRIS), Tohoku University, Sendai 980-8577, Japan

[c] WPI Advanced Institute for Materials Research, Tohoku University, Sendai 980-8577, Japan

[d] School of Physics, University of Electronic Science and Technology of China, Chengdu, Sichuan 611731, P. R. China

[e] School of Chemistry and Chemical Engineering, Shanghai Jiao Tong University, Shanghai 200240, P. R. China

[f] Department of Materials Science and Engineering, Johns Hopkins University, Baltimore, Maryland 21218, United State

*** Corresponding authors**

E-mail address: panliu@sjtu.edu.cn (P. Liu) , mwchen@jhu.edu (M.W. Chen).

Experimental Section

1. Materials synthesis

1.1 Fabrication of nitrogen doped nanoporous graphene (NG)

NG was fabricated by a chemical vapor deposition (CVD) process using dealloyed nanoporous nickel as substrates and catalysts for growing graphene. Specifically, a $Ni_{30}Mn_{70}$ (atomic ratio) ingot, obtained by an arc-melting method, was cold-rolled to $Ni_{30}Mn_{70}$ sheets with the thickness of 150 μm. Nanoporous Ni templates were prepared by chemical dealloying in 1M $(NH_4)_2SO_4$ aqueous solution at 50°C for 5h[1], followed by thoroughly rinsing with deionized water and ethanol. After drying in the vacuum oven at room temperature, the nanoporous Ni template with proper size was loaded into a quartz tube (φ50 × φ50 × 1400 mm) of a three-heating zone furnace. Melamine was used as the carbon and nitrogen sources for growing N-doped nanoporous graphene. As displayed in Figure S1, the nanoporous Ni and ~0.25g melamine powders loaded in a ceramic boat was separately placed in the left and central heating zone. The left heating zone was first heated from room temperature to 800 °C within 40 minutes to anneal nanoporous Ni under the mixed gas atmosphere of Ar (200 sccm) and H_2 (200 sccm). Meanwhile, the central heating zone was gradually ramped to 200°C within 40 minutes. During the 5 minutes pre-reduction annealing, melamine powders were further heated to 300°C. When the temperature of central heating zone approaches 300°C, melamine powders start to evaporate and form continuous graphene film on the Ni substrate. The optimal graphene growth time was 7 minutes. The furnace was then immediately opened and cooled down to room temperature using a fan. After etching away the Ni substrates using 2.0M HCl mixed with ferric chloride ($FeCl_3$) at 50°C for overnight and subsequently rinsed with deionized water for 5 times, N doped nanoporous graphene can be obtained by a freeze-drying technique.

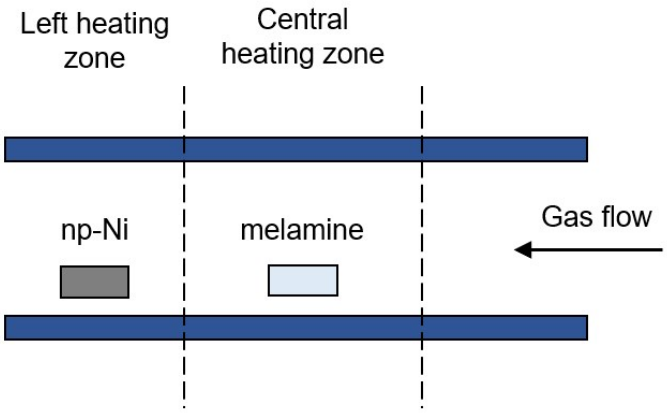

Fig. S1 schematic illustration of NG growth process.

1.2 Fabrication of Cu-NG

A standard high temperature gas transportation process was employed to fabricate Cu-NG, NG and cuprous oxide (Cu_2O) as illustrated in Figure S2. Ceramic boats loaded with NG and Cu_2O were placed at different heating zones. Then, NG and Cu_2O were heated to 950 °C and 1050 °C, respectively, for 2h at the heating rate of 5 °C/min under the Ar flowing (50 sccm) to yield Cu-NG.

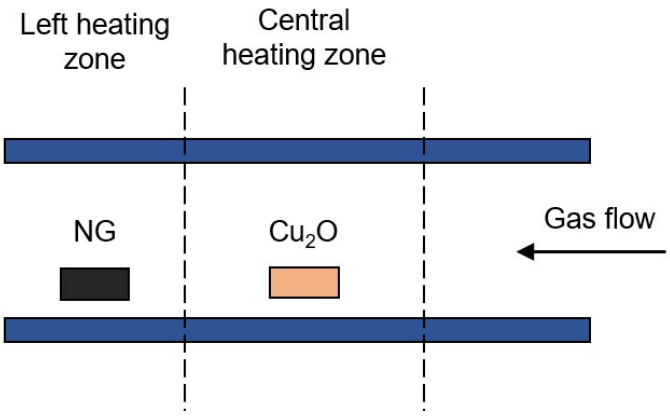

Fig. S2 schematic illustration of the fabrication of Cu-NG.

1.3 Fabrication of (Ni,Cu)-NG

The fabrication procedure of (Ni,Cu)-NG was the same as that of Cu-NG except that the NG supports contained residual single-atom Ni (denoted as Ni-NG)stead. After the CVD process to grow N doped graphene, the sample was etched with 2M HCl without $FeCl_3$ at room temperature for 10h.

2. Structure Characterizations

The porous morphology of nanoporous nickel and graphene was characterized by a scanning electron microscope (SEM, FEI 3D Versa). High-resolution TEM (HRTEM) images of all samples were obtained by JEOL ARM 200F equipped with an aberration corrector for the image-forming objective lens operating at 200 kV acceleration voltage. The high-angle annular dark-field scanning transmission electron microscopy (HAADF-STEM) images were obtained by JEOL ARM 200F equipped with an aberration corrector for the probe-forming lens and an energy-dispersive X-ray spectrometer (EDS). The EELS mappings were performed using a *Gatan* EELS system on the STEM mode. The Raman spectra were collected by a Raman spectrometer (Renishaw inVia Qontor) with the incident wavelength of 532 nm and the low laser power of 5 mW. The chemical compositions of the samples were investigated by X-ray photoelectron spectroscopy (XPS) utilizing AXIS UltraDLD XPS system (Kratos). Extended

X-ray absorption fine structure (EXAFS) measurements were conducted on the BL14W1 beamline at Shanghai Synchrotron Radiation Facility (SSRF). The X-ray diffraction (XRD) data was record on a D8 ADVANCE DaVinci X-ray powder diffractometer (XRD) using Cu Kα radiation from 20° to 70°. The XRD scan rate is 2° min $^{-1}$.

3. Electrochemical tests

All electrochemical tests were carried out in a standard three-electrode cell using electrochemical station (Pine Research Instrumentation, USA) equipped with a rotating ring disk electrode (RRDE) at room temperature. In the three-electrode cell system, a platinum wire, a Ag/AgCl (3 M KCl) electrode and the rotating ring disk electrode loaded with our catalyst inks were used as the counter electrode, reference electrode and working electrode, respectively. All the electrocatalytic reactions were evaluated in oxygen/nitrogen-saturated 0.1M KOH aqueous solution and all the potential given in this work were converted to reversible hydrogen electrode (RHE) on the basis of the following equation:

$$E(RHE) = E(Ag/AgCl) + 0.210 + 0.0591\text{pH}$$

To prepare the catalyst inks, 2 mg catalysts were blend with 200 μL Nafion solution (0.5 wt% in ethanol) and then sonicated for about half an hour to form homogeneous catalyst inks. Subsequently, 9 μL as-prepared inks were loaded onto the RRDE with the electrode surface of about 0.2471 cm^2 and dried at ambient temperature. The loading amounts were determined to be about 0.36 mg cm^{-2}. The cyclic voltammetry (CV) measurements were conducted at the sweep rate of 100 mV s^{-1}. The Linear sweep voltammetry (LSV) measurements were implemented at various rotating speeds from 400 rpm to 2025 rpm with a sweep rate of 10 mV s^{-1}. The RRDE measurements were carried out at the rotating speed of 1600 rpm and the electron transfer number (n) and H_2O_2 yield can thus be calculated according to following equations:

$$\%H_2O_2 = 200\, I_r / \text{N}(I_d + I_r/\text{N})$$

$$n = 4I_d / (I_d + I_r/\text{N})$$

Where I_r and I_d are the ring current and the disk current, and N is the current collection efficiency in RDDE (N = 0.37). For the electrochemical accelerated durability testing (EADT), the durability of the catalyst was tested with applied potential ranging from 0.2 V to 1.0 V (versus RHE) at the sweep rate of 100 mV s^{-1}. The rechargeable Zn-air battery was assembled according to the typical configuration. The anodes and air cathodes were the polished 0.3 mm Zn foils and the carbon papers loaded with 1 mg/cm^2 corresponding catalysts (a mixture of Pt/C

+ IrO2 or (Ni,Cu)-NG), respectively. 6.0 M KOH with 0.1 M ZnCl2 solution was used as the electrolyte.

4. DFT computational details

DFT calculations have been performed using the Vienna *ab* initio simulation package (VASP)[2] with the projector-augmented wave (PAW)[3] method. All calculations were based on the same generalized gradient approximation (GGA) method with Perdew-Burke-Ernzerhof (PBE)[4] functional for the exchange-correlation term. The plane wave cutoff was set to 400 eV. The Brillouin zone integration was carried out with 2×2×1 Monkhorst-Pack *k*-point grid. The convergence of energy and forces were set to 5×10^{-7} eV and 0.01 eV $Å^{-1}$ for structure optimization, respectively.

A periodically repeated single-layer graphene model with Ni-N_3 and Cu-N_2C_2 structures embedded in the in-plane matrix has been built to simulate the Ni/Cu co-anchored catalysts with a vacuum slab height of 20 Å, the graphene models doped with Ni-N_3 or Cu-N_2C_2 have also been studied. All atoms of the catalysts and adsorbates were fully relaxed during calculations.

The associative ORR pathway can be summarized as follows:

$$\text{Overall: } O_2 + 2H_2O + 4e^- \rightarrow 4OH^-$$

$$O_2 + * + H^+ + e^- \rightarrow OOH^*, \qquad \Delta G_1$$

$$OOH^* + H^+ + e^- \rightarrow O^* + H_2O, \qquad \Delta G_2$$

$$O^* + H^+ + e^- \rightarrow OH^*, \qquad \Delta G_3$$

$$OH^* + H^+ + e^- \rightarrow H_2O + *, \qquad \Delta G_4$$

The free energy of the adsorption of intermediates including OH*, O* and OOH* is calculated by: $G = E^{DFT} + ZPE - T\Delta S$, where E^{DFT} is the DFT-optimized total energy, ZPE is the zero-point vibrational energy, T is the temperature, and ΔS is the entropy[5]). The zero-point energies and entropies of the reaction species were calculated from the vibrational frequencies. During these frequency calculations, all atoms of substrate were rigidly constrained so that no additional degrees of freedom, due to the catalyst, are introduced in to the reacting system.

$$\text{Onset potential} = -\max(\Delta G_1, \Delta G_2, \Delta G_3, \Delta G_4) / e.$$

The Ni-N_3 model, three C atoms around the Ni atom in graphene lattice were all replaced by N atoms, while in the initial Cu-N_2-V model, only two N atoms around the Cu atoms were replaced by C atoms, and one C atom site was set to be vacant. As suggested by previous

research[6], carbon vacancies were inclined to be introduced in the process of copper oxide reduction on the carbon matrix at high temperatures. After the structural optimization, there was no obvious structural change of the Ni-N_3 system except that the distance between Ni atoms and N atoms was shortened from 1.695 Å to 1.681 Å. However, for Cu-N_2-V model, the C vacancy in the Cu-N_2-V model disappeared after structural relaxation, and Cu atom leaned against neighboring C atoms around the vacancy and formed a Cu-N_2-C_2 configuration.

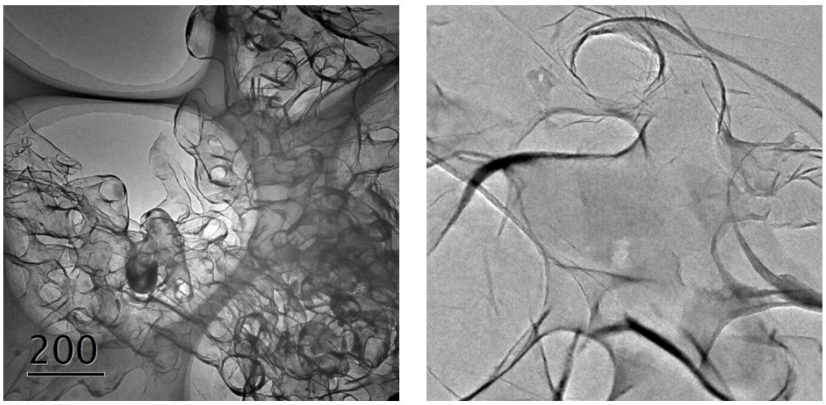

Fig. S3 TEM image of nanoporous graphene showing the well-retained nanoporous morphology after the high temperature gas transportation process.

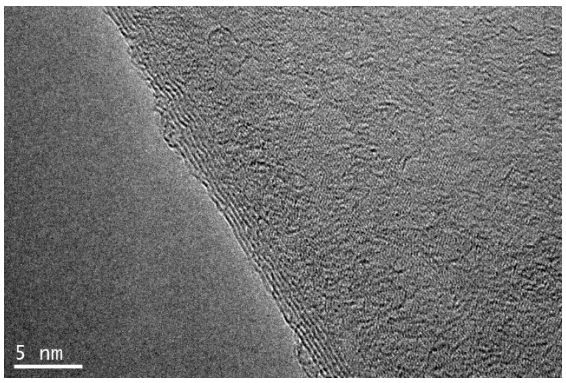

Fig. S4 HRTEM image of (Ni,Cu)-NG revealing the nature of few-layer graphene.

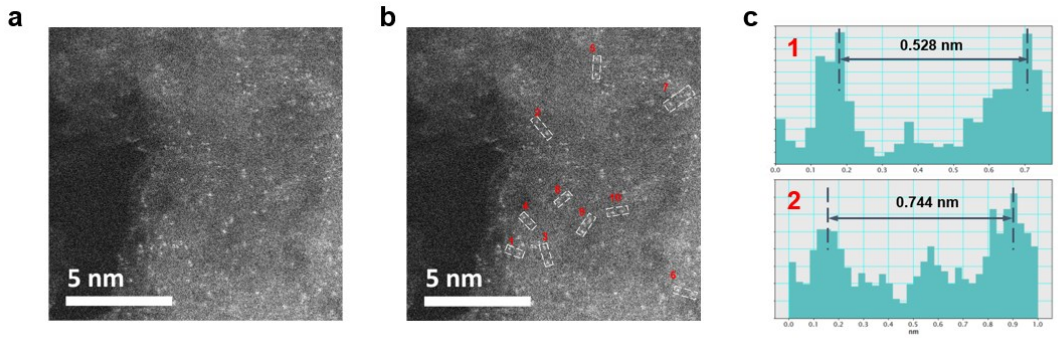

Fig. S5 (a, b) cs-corrected HAADF-STEM image of (Ni,Cu)-NG. Several single atoms and their neighboring single atoms are highlighted by white rectangle. (c) The intensity profile of the corresponding single atom and its neighboring single atom.

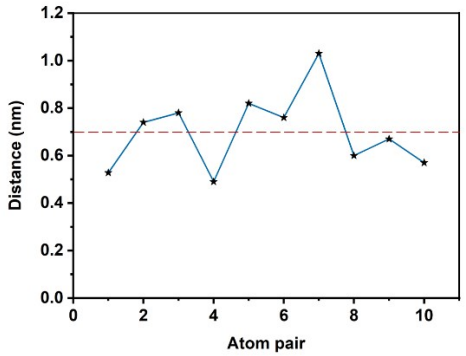

Fig. S6 The distance between single atoms and their neighboring single atoms.

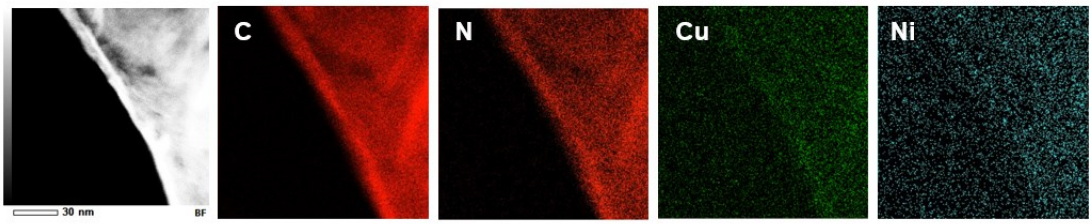

Fig. S7 EDS mapping result of (Ni,Cu)-NG with extended sampling time.

=

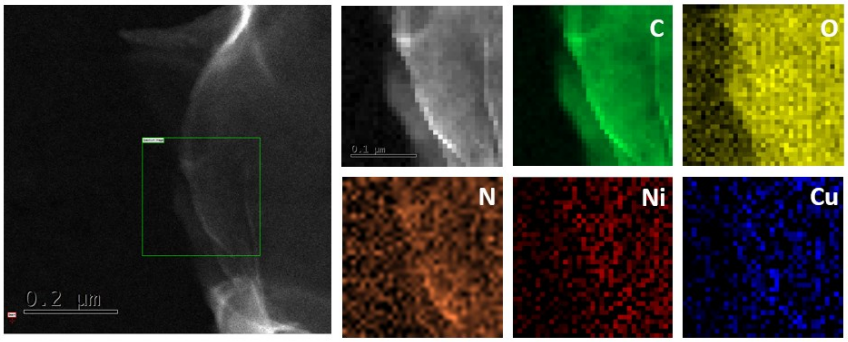

Fig. S8 Electron energy loss spectroscopy (EELS) mappings of the element distribution of C (green), O (yellow), N (brown), Ni (red) and Cu (blue).

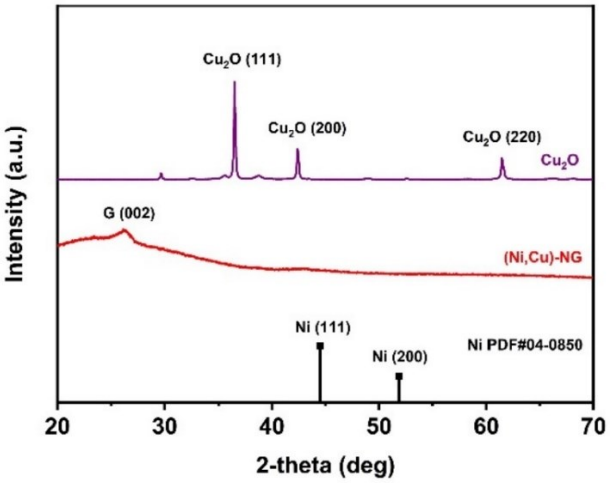

Fig. S9 XRD pattern of (Ni,Cu)-NG.

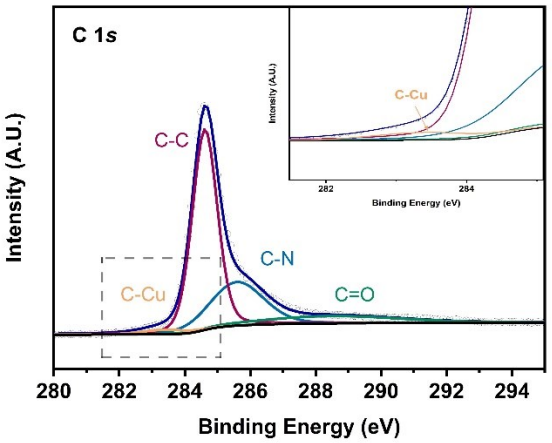

Fig. S10 High resolution C 1*s* XPS spectrum of (Ni,Cu)-NG.

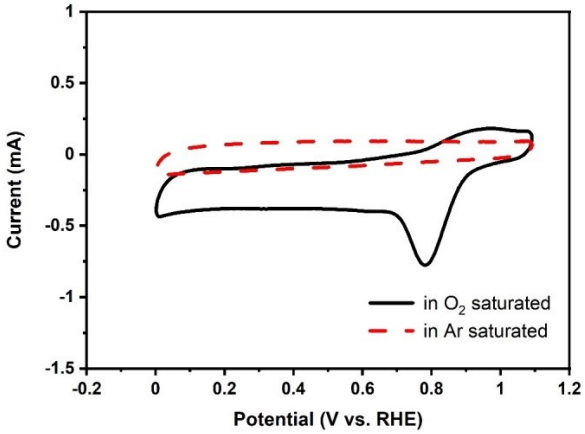

Fig. S11 CV curves of (Ni,Cu)-NG in 0.1M oxygen-saturated KOH (solid line) and argon-saturated KOH (dash line).

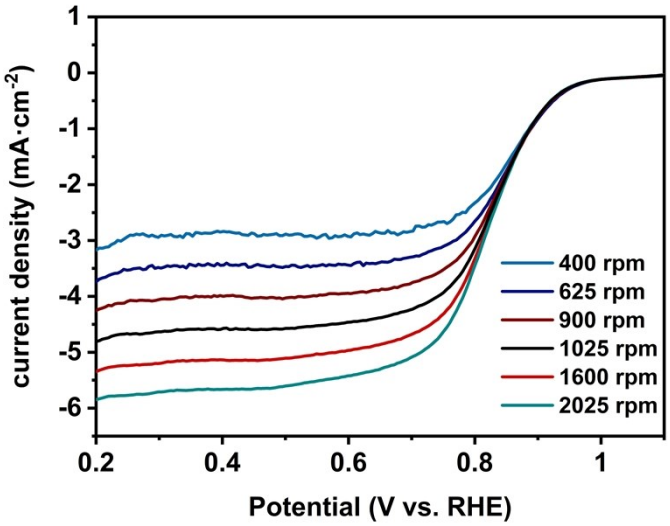

Fig. S12 Polarization curves of Pt/C at different rotating speed ranging from 400 to 2025 rpm, which we used for the kinetics current calculation.

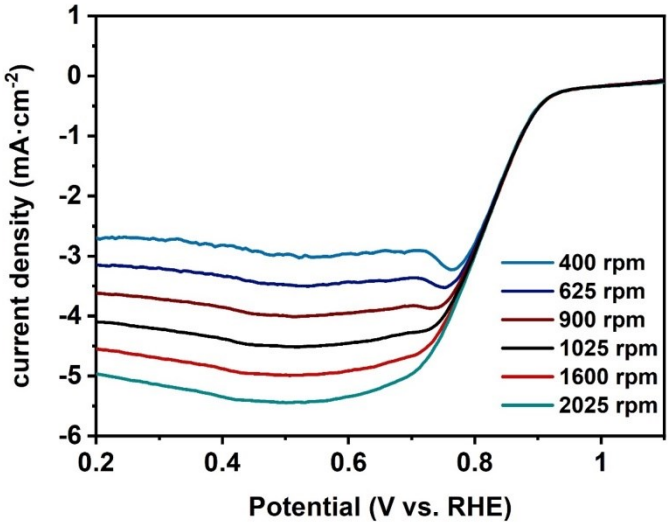

Fig. S13 Polarization curves of Cu-NG at different rotating speed ranging from 400 to 2025 rpm.

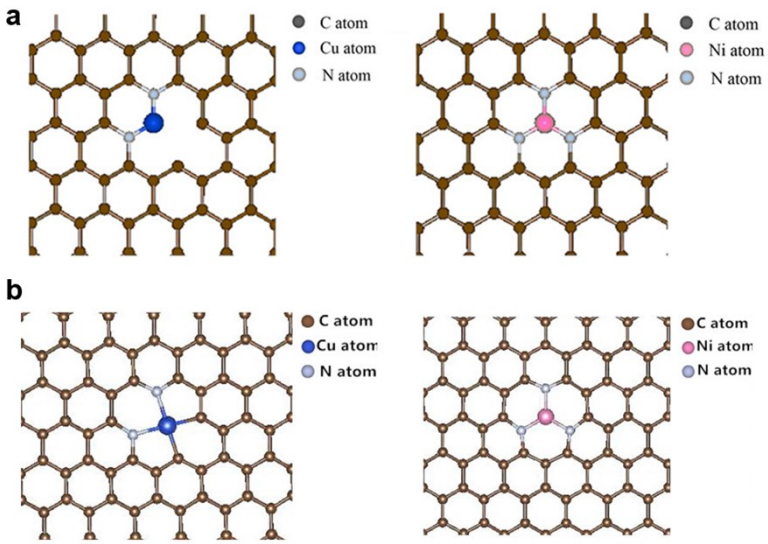

Fig. S14 (a, b) Ni-N_3 and Cu-N_2-V models before structural relaxation (a) and after relaxation (b).

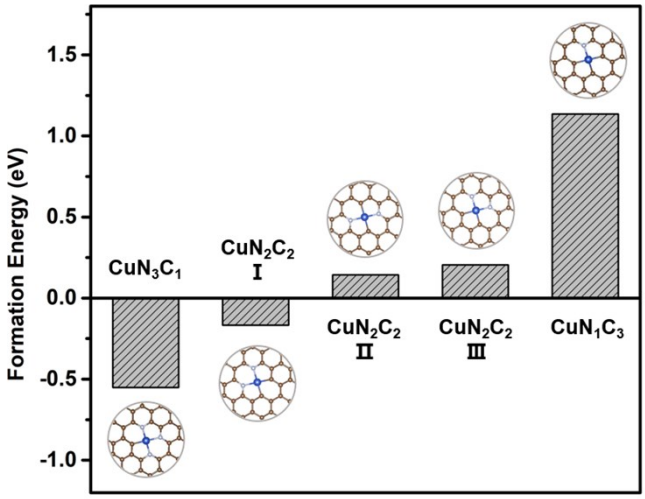

Fig. S15 Formation energy of different CuN_xC_{4-x} (x=1,2,3) structure.

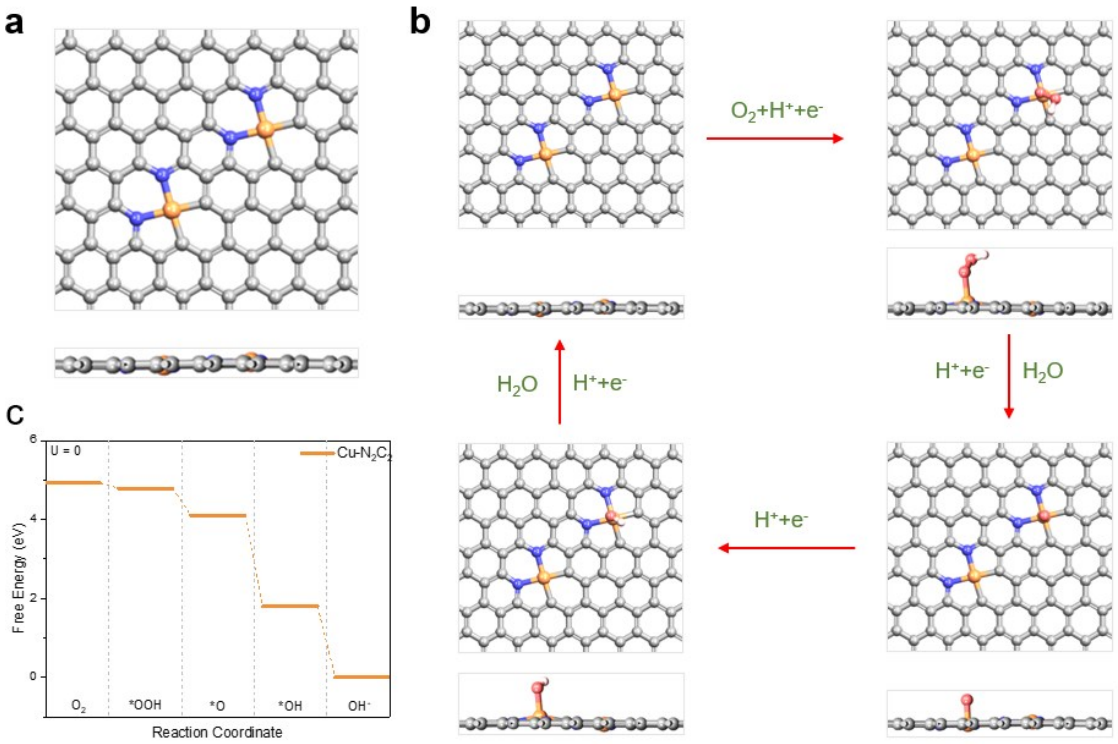

Fig. S16. Theoretical investigation of ORR activity on Cu@Cu-NG active sites. (a) Top and side views of structure model with Cu@Cu-NG active sites. Red: O; white: H. (b) Top and side views of adsorption configurations of each intermediates during ORR process on Cu@Cu-NG active sites. (c) Free energy profile of ORR on Cu-N_2-C_2 active sites.

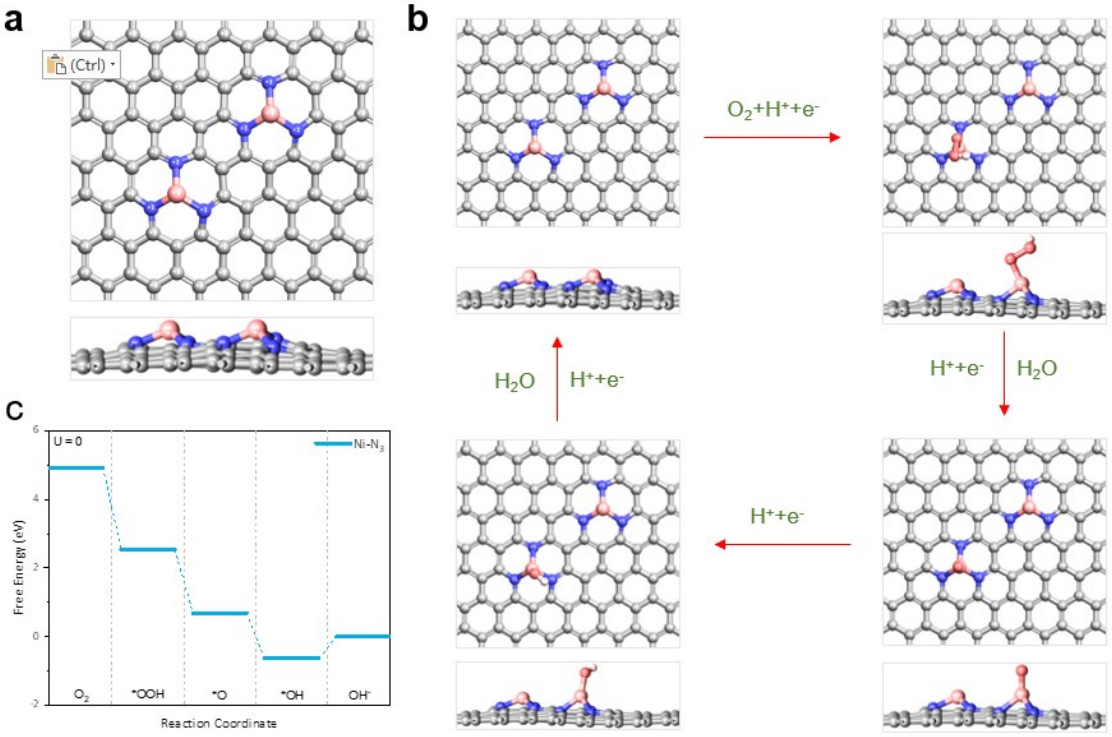

Fig. S17 Theoretical investigation of ORR activity on Ni@Ni-NG active sites. (a) Top and side views of structure model with Ni@Ni-NG active sites. (b) Top and side views of adsorption configurations of each intermediates during ORR process on Ni@Ni-NG active sites. (c) Free energy profile of ORR on Ni@Ni-NG active sites.

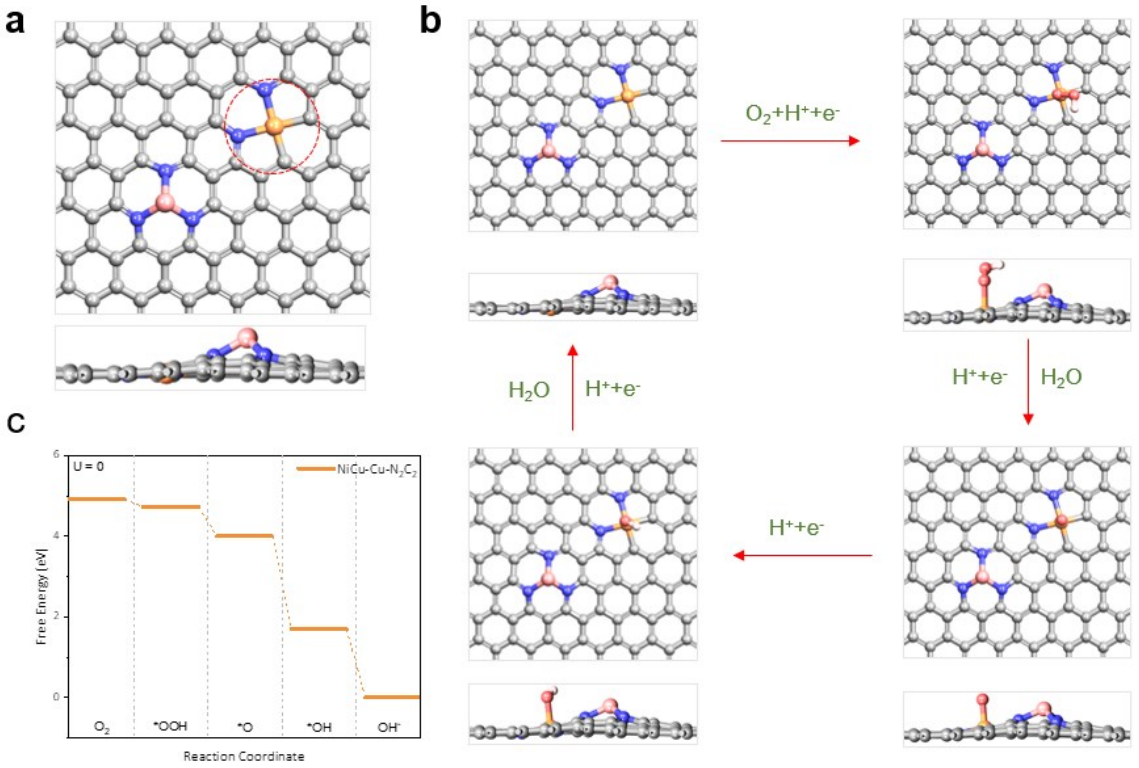

Fig S18. Theoretical investigation of ORR activity on Cu@NiCu-NG active sites. (a) Top and side views of structure model with Cu@NiCu-NG active sites. (b) Top and side views of adsorption configurations of each intermediates during ORR process on Cu@NiCu-NG active sites. (c) Free energy profile of ORR on Cu@NiCu-NG active sites.

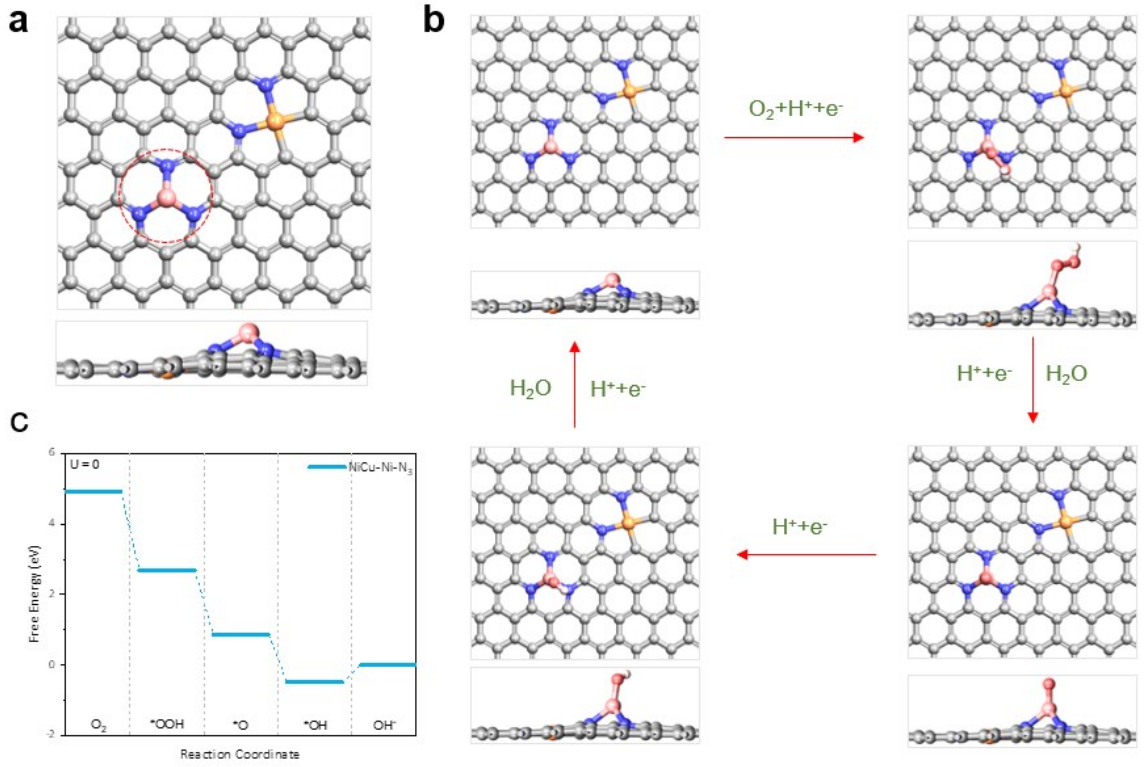

Fig.S19 Theoretical investigation of ORR activity on Ni@NiCu-NG active sites. (a) Top and side views of structure model with Ni@NiCu-NG active sites. (b) Top and side views of adsorption configurations of each intermediates during ORR process on Ni@NiCu-NG active sites. (c) Free energy profile of ORR on Ni@NiCu-NG active sites.

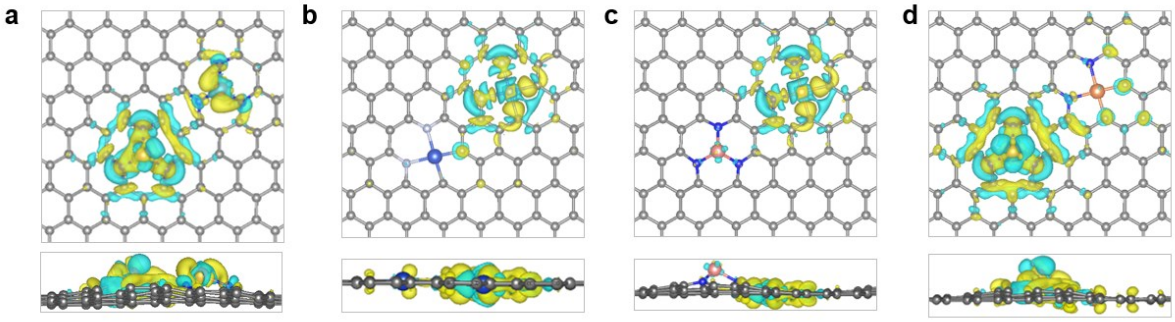

Fig.S20. Differential charge density analysis of different active sites. (a) Top and side views of differential charge density of Ni@Ni-NG active sites. (b) Top and side views of differential charge density of Cu@Cu-NG active sites. (c) Top and side views of differential charge density of Cu@NiCu-NG active sites. (d) Top and side views of differential charge density of Ni@NiCu-NG active sites.

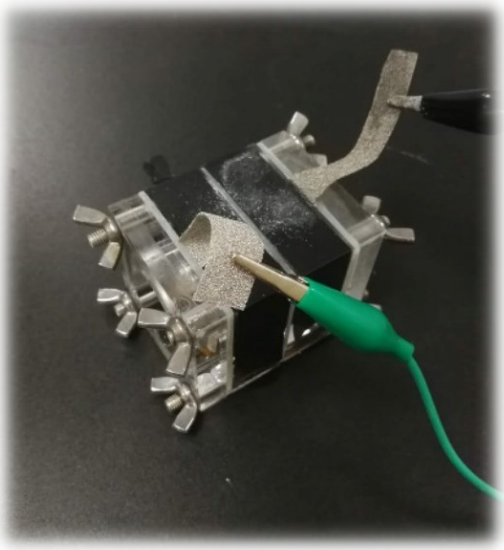

Fig. S21 Digital photograph of the assembled homemade Zn-air battery.

Fig. S22 Photograph showing the open-circuit voltage of the (Ni,Cu)-NG based Zn–air battery.

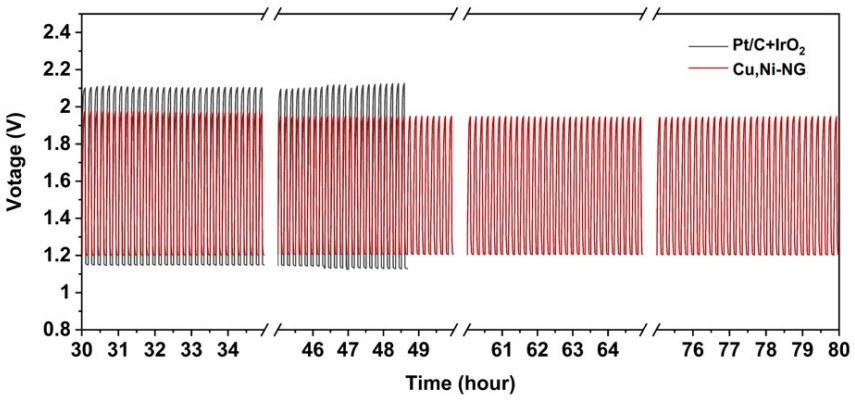

Fig. S23 Charge and discharge cycling plots of Pt/C+IrO_2 based and (Ni,Cu)-NG based Zn-air batteries at 10 mA cm^{-2}.

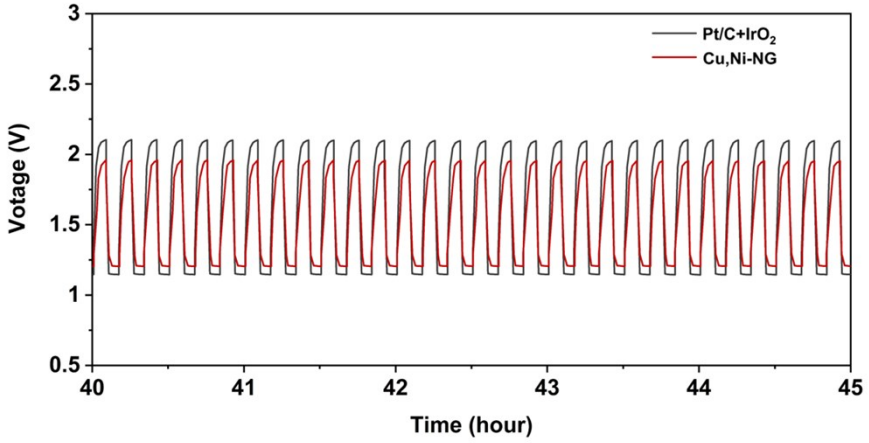

Fig. S24 Magnification of the particular region in change and discharge cycling plots of Pt/C+IrO_2 based and (Ni,Cu)-NG based Zn-air batteries at 10 mA cm^{-2}.

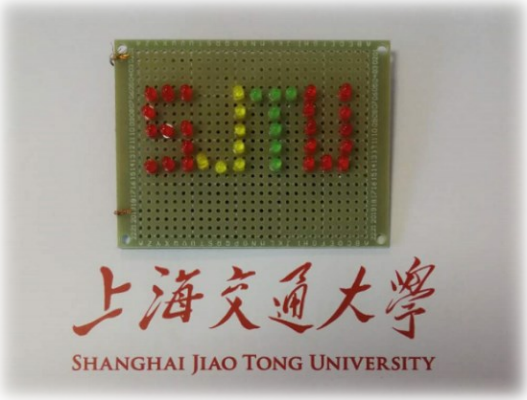

Fig. S25 Digital photograph of the LED array powered by the (Ni,Cu)-NG based Zn-air battery.

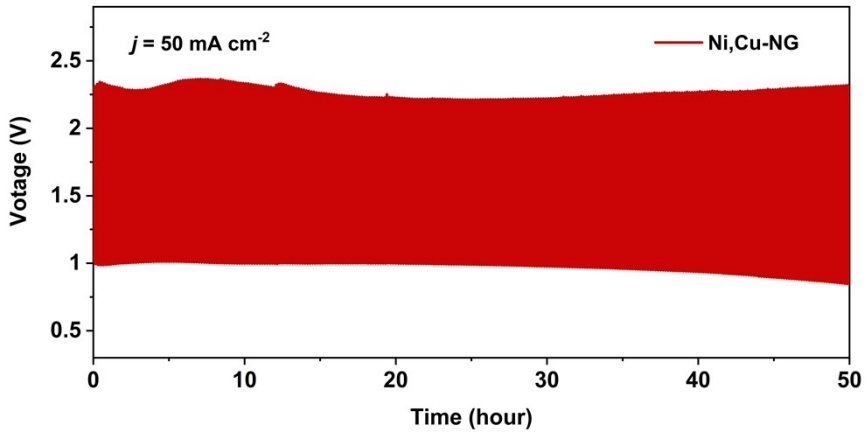

Fig. S26 Charge and discharge cycling curves of the (Ni,Cu)-NG based Zn-air battery operated at the high current density of 50 mA cm^{-2}.

Table S1 ICP results of (Ni,Cu)-NG and Cu-NG

Sample	Ni (wt%)	Cu (wt%)
(Ni,Cu)-NG	0.596	1.534
Cu-NG	0.102	1.745
Ni-NG	0.540	/

Table. S2 Onset potential of different catalytic active sites from DFT calculations

Active Sites	Onset Potential (V)
Cu@Cu-NG	0.13
Ni@Ni-NG	-0.64
Cu@NiCu-NG	0.19
Ni@NiCu-NG	-0.49

Table S3 EXAFS fitting results of (Ni,Cu)-NG.

Sample	Scattering path	CN	R(Å)	σ^2 (10^{-3}Å^2)	ΔE_0(eV)	R factor
(Ni,Cu)-NG	Ni-N	3.1	1.87	2	-5.6	0.006
	Cu-N	2.2	1.96	4.6	2.7	0.015
	Cu-C	1.9	1.94	4.3	2.6	

Table S4 Summary of recent reported ORR electrocatalytic performance of carbon based materials.

Catalyst	Catalyst loading (mg/cm2)	ORR Half-wave Potential (V vs. RHE)	Reference
(Ni,Cu)-NG	0.36	0.840	**This work**
Fe1-HNC-500-850	0.2	0.842	Adv. Mater. 2020,32,1906905
10Co-N@DCNF	0.1	0.83	Angew. Chem. Int. Ed. 2020,59,6122
Fe-N/P-C-700	0.6	0.867	J. Am. Chem. Soc. 2020, 142, 2404
Ni-N4/GHSs/Fe-N4	0.26	0.83	Adv. Mater. 2020. 32. 2003134
Ni-NHGF	0.275	0.82	Nat. Catal. 2018,1,63
FeNx/C	0.6	0.82	J. Am. Chem. Soc. 2014, 136,10882
Fe-N/C-800	0.1	0.80	J. Am. Chem. Soc. 2014,136, 1102
(Fe-P)nMOF	0.16	0.81	J. Am. Chem. Soc. 2012, 134, 6707
Co3O4/N-rGO	0.17	0.83	Nat. Mater. 2011, 10, 780
pCNT@Fe1.5@GL	0.2	0.81	Adv. Mater. 2017,29, 1606534
CoII-A-rG-O	0.6	0.81	Angew. Chem. Int. Ed. 2015, 54, 12622
Fe/N/C HNSs	0.255	0.77	Nanoscale 2015, 7, 1501
Fe3C@NG800-0.2	0.2	0.82	ACS Appl. Mater. Inter. 2015,7, 21511
Fe-N-C/rGO	0.35	0.81	ACS Appl. Mater. Inter. 2018, 10, 2423
Fe-NCCs	0.1	0.82	ACS Appl. Energ. Mater. 2018, 1, 4982
Fe@N-C-12	0.311	0.81	ACS Catal. 2017,7, 7638
Fe0.25-N/C-900	0.2	0.812	Nano Energy 2017, 36, 286
CoMn/pNGr	0.8	0.79	ACS Catal. 2017, 7, 6700

MCO/CNFs@NC	0.13	0.76	ACS Appl. Energy Mater. 2018, 1, 1612
N/MCNS-800	0.2	0.82	Chem. Commun. 2017, 53, 11568

Table S5 Summary of recent reported carbon-based Zn-air battery performance

Catalyst	**Catalyst Loading (mg/cm2)**	**Peak Power Density (mW/cm2)**	**Durability (h)**	**Reference**
(Ni,Cu)-NG	1	150.6	＞90	**This work**
Co-N,B-CSs	0.5	100.4	＞128	ACS Nano 2018, 12, 1894
Co-Nx-C	0.5	152	60	Adv. Mater. 2017, 29, 1703185
CoNi-SAs/NC	1.4	101.4	＞30	Adv. Mater. 2019, 31,1905622
FeNC-S-Fe_xC/Fe	0.2	150	44	Angew. Chem. Int. Ed. 2018, 57, 1856
Fe-N/P-C-700	3.0	133.2	40	J. Am. Chem. Soc. 2020, 142, 2404
NiCo2S4@gC3N4-CNT	2.33	142	＞100	Adv. Mater. 2019, 31,1808281
N-GRW	0.5	65	30	Sci. Adv. 2016, 2, e1501122
NLPC	0.5	232	36	Angew. Chem., Int. Ed. 2018, 57, 8614
N-CNT/CoO-NiO-NiCo	0.53	102	16.7	Angew. Chem. Int. Ed. 2015,
Fe-NSCNT	1	130.2	46	J. Alloy Compd., 2020, 848, 156367

Co-N-CNT	1	101	15	Adv. Funct. Mater., 2018, 28, 1705048
CoZn-NC-700	1.2	152	62.5	Adv. Funct. Mater., 2017, 27, 1700795
Meso/micro FeCo-Nx-CN-30	2.0	150	44	Angew. Chem. Int. Ed., 2018, 57, 1856
Fe-N/P-C-700	3.0	133.2	40	J. Am. Chem. Soc., 2020, 142, 2404

References

1. H. J. Qiu, J. Kang, P. Liu, A. Hirata, T. Fujita, M. Chen, J. Power Sources **2014**, 247, 896
2. G. Kresse and J. Furthmüller, Phys. Rev. B, **1996**, 54, 11169-11186.
3. P. E. Blöchl, Phys. Rev. B, **1994**, 50, 17953-17979.
4. J. P. Perdew, K. Burke and M. Ernzerhof, Phys. Rev. Lett., **1996**, 77, 3865-3868
5. J. K. Nørskov, J. Rossmeisl, A. Logadottir, L. Lindqvist, J. R. Kitchin, T. Bligaard, H. Jónsson, J. Phys. Chem. B, **2004**, 108, 17886-17892.
6. Z. Yang, B. Chen, W. Chen, Y. Qu, F. Zhou, C. Zhao, Q. Xu, Q. Zhang, X. Duan, Y. Wu, *Nat. Commun.* **2019***, 10,* 3734.